# Accounting for the Effects of Widespread Discrete Clutter in Subsurface EMI Remote Sensing of Metallic Objects

Kevin O'Neill, *Member, IEEE*, Keli Sun, *Member, IEEE*, Fridon Shubitidze, *Member, IEEE*, Irma Shamatava, and Keith D. Paulsen, *Member, IEEE*

***Abstract*—In practice, most signal processing strategies for discrimination of buried objects are clutter limited. This applies even to discrimination of shallow sizable metallic objects, such as unexploded ordnance (UXO), which are to be found predominantly in the top meter of soil. The environment typically features widespread metallic clutter from detonated ordnance or other sources. Such fragments can be numerous and are often shallower than the objects of interest. Currently, the preeminent remote sensing mode for buried UXO is ultrawideband electromagnetic induction (EMI), operating over part or all of the band from some tens of hertz up to perhaps hundreds of kilohertz. Particularly because EMI fields fall off sharply with range, signals from shallow clutter may be relatively strong and can easily obscure essential scatterer signatures. To treat this, a rational theory of EMI scattering from widespread metallic clutter is formulated and tested. For dense, well-distributed clutter, analytical rules are derived for dependence of signal strength on sensor elevation, under various fundamental excitation types. For more erratic, sparse clutter distributions, signal statistics from Monte Carlo simulations show patterns like those from the analytical rules. The dependence of clutter signal magnitude on antenna elevation is determined for both thin surface layers and for volume layers of widespread small items, and for both dense and sparse clutter distributions. These are contrasted with the patterns expected from single, larger, discrete objects of interest, and the contrast is exploited in discrimination exercises for the screening problem. For sparse clutter distributions, results from inversion processing formulations that account for the patterns of clutter statistics are compared to simple least squares treatments.**

***Index Terms*—Clutter, electromagnetic induction (EMI), subsurface, unexploded ordnance (UXO).**

## I. Introduction

UNEXPLODED ordance (UXO) cleanup is currently a widespread and extremely expensive environmental problem. In practice, clutter dominates the problem and contributes to unacceptably high false-alarm rates. Objects of interest ("targets") may be missed when clutter screens the object sought or distorts essential signatures. Thus, decision thresholds must be set high, since it is urgent to find as many UXO as possible, ideally all. The result of this is that most UXO cleanup resources are consumed by excavation of innocuous metallic items. Perhaps the most promising subsurface sensing technology for UXO discrimination is broadband electromagnetic induction (EMI), e.g., [1]–[4]. This technology operates in the band between a few hertz and some hundreds of kilohertz where electromagnetic phenomena are magneto-quasi-static, consisting of diffusion fields and not waves. Transmitted ("primary") magnetic fields that impinge upon metallic scatterers are able to penetrate them, at least to some degree. The primary fields elicit magnetic dipole type responses via induced current loops or induced magnetization of constituent materials. The resulting scattered or "secondary" fields depend thus on material types as well as geometry and disposition of the object. Shallow subsurface remote sensing in this band has the advantage that the soil is typically transparent to the transmitted and scattered fields. A burgeoning of investigation, analysis, and testing has accompanied the latest generations in EMI sensors [5]–[12]. While some of the approaches are statistical, virtually all inversion and classification processing is based on the assumption of relatively simple models for both the target and its environment.

Here we pursue explicitly the signal behavior of a clutter environment consisting of widespread small metallic fragments. "Small" simply means that each clutter item has dimensions significantly less than that of the overall problem geometry, including antenna height, depths of interest, and scatterers of real interest, e.g., a UXO. "Widespread" means that a number of clutter items appear within the sensor's field of view at any time, and the clutter is distributed over the entire domain surveyed, though possibly only at a discrete depth. The clutter distributions are further divided into the classes of dense distributions or well-distributed assemblages, on the one hand, and sparse distributions on the other. In the former case, the items are small and widespread enough so that we assume that any surface or volume subregion contains a statistically representative collection of them. Sparse distributions produce more erratic signals, and for them we focus on the statistics of response, drawing parallels to behavior of the well-distributed case.

Fig. 1 illustrates dense distributions, showing manually randomized arrangements of spheres and small cylinders. A particular model of the GEM-3 ultrawideband (UWB) EMI sensor head [1] is shown with the sphere distribution. This instrument was used for all measurements reported here. It operates between about 30 Hz and 50 kHz, consisting of concentric transmission and receiver coils all in the plane of the head. The

Manuscript received April 7, 2004; revised September 16, 2004. This work was supported in part by the Strategic Environmental Research and Development Program and in part by the U.S. Army Corps Engineers Engineer Research and Development Center AF25 program.

K. O'Neill is with the U.S. Corps of Engineers, Engineer Research and Development Center, Cold Regions Research and Engineering Laboratory, Hanover, NH 03755 (e-mail: Kevin.ONeill@ERDC.usace.army.mil).

K. Sun, F. Shubitidze, I. Shamatava, and K. D. Paulsen are with the Thayer School of Engineering, Dartmouth College, Hanover, NH 03755 USA.

Digital Object Identifier 10.1109/TGRS.2005.858437

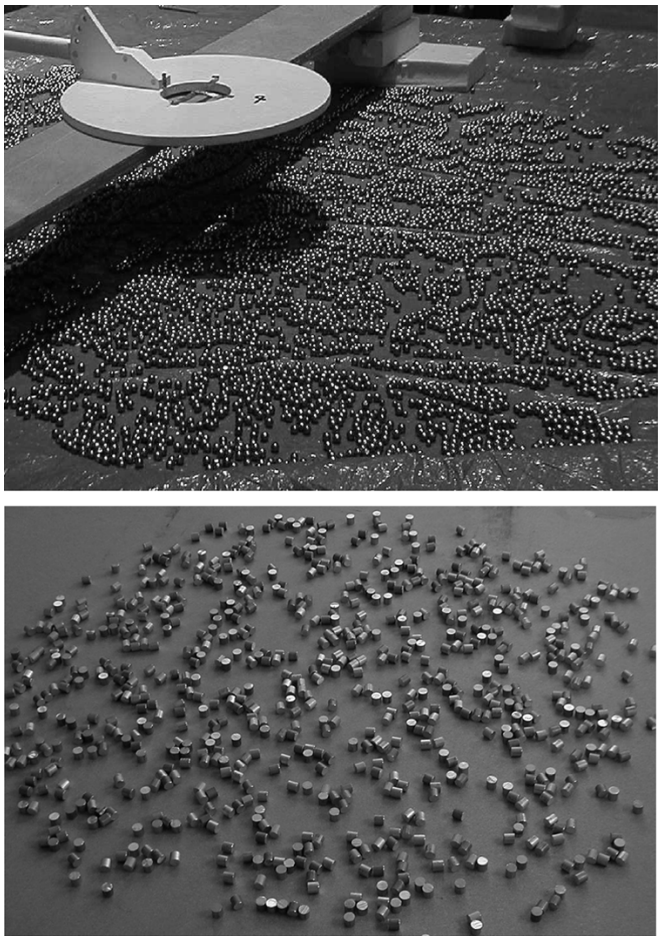

Fig. 1. (Top) Forty-centimeter-diameter GEM-3 sensor head above a manually randomized dense surface distribution of steel spheres. (Bottom) Similarly randomized dense distribution of short aluminum cylinders spread across about a 1.2-m square area.

electric currents in the two outer transmitting coils circulate in opposite directions. This produces a nonzero primary magnetic field $H^{\mathrm{PR}}$ at some distance from the head. At the same time, the two fields are scaled so that they approximately cancel one another in the central cavity of the sensor head. The receiver coil surrounds this cavity and therefore responds predominantly to the scattered fields originating outside the sensor. The sensor responses are retained in the form of two components, one in-phase with the transmitted field ("real" component) and the other in-phase quadrature with the primary field ("imaginary" component). Given knowledge of the sensor coil geometry and currents, the primary field from this device is readily calculated. Fig. 2 shows an example sparse clutter distribution, consisting of more diverse, widely scattered items. Referring to the marked points at 10-cm separation, one sees that the object separation is some significant fraction of the sensor head diameter.

The question arises: should we expect a cloud of small clutter items to produce a strong enough signal to matter, relative to that from a much more massive object of interest? Other things being equal, small items will produce much smaller EMI responses. A quite approximate but still useful rule of thumb is that, at least from some reasonable range, compact objects with comparable composition subject to the same excitation will produce responses in proportion to their volume. By this standard, an item with, say, one-tenth the diameter of another would only produce $1/1000$ as strong a response. Nevertheless, clouds of small items can still pose problems because 1) there may be many, possibly very many small items, the extreme being nearly invisible but densely distributed microfragmentation; and 2) clutter items may be near the surface, much closer to the sensor. EMI sensors for close interrogation, i.e., discrimination, typically transmit from wire loops that we may approximate as magnetic dipoles. The transmitted signal decays as $1/R^3$, where R is the distance to a scatterer. Similarly, the impinging primary field induces a dipole type response in the scatterer, and its reradiated field also decays as $1/R^3$ as it returns to the sensor. (We assume here and in what follows that the transmitter and receiver are colocated). Altogether, this produces the commonly used EMI $1/R^6$ signal decay rule of thumb for dipole type sensors and scatterers. This rule implies that a near-surface object one-tenth as far from the sensor as a deeper object will produce one million times the signal magnitude, other things being equal. Thus, a distribution of small clutter items near the surface may obscure a larger, deeper item of interest, even though the inherent response of each clutter item is very much smaller.

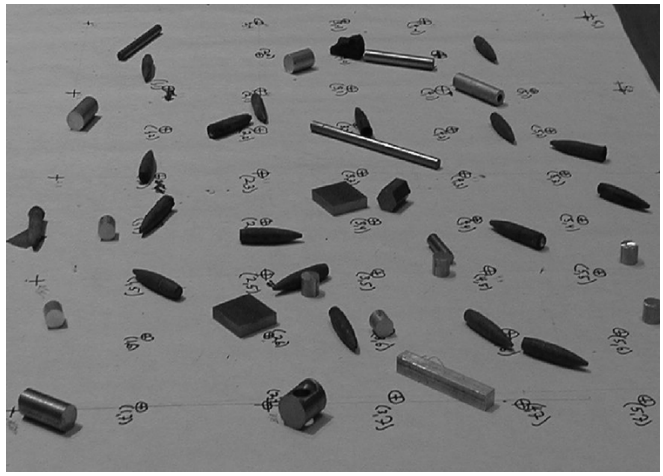

Fig. 2. Sparse distribution of clutter items, some collected from firing ranges, relative to 10-cm spacing of grid marks.

The tasks here are to produce an analytical rendering of the physics and phenomenology of EMI scattering by widely dispersed small items, and then to implement those results in a measurement and processing framework. Particular attention is paid to the spatial dependence of frequency response for different clutter and scatterer configurations. That is, drawing upon both frequency and positional variation produces a beneficial expansion of data diversity. Specific patterns and statistics in the linkage between spatial and frequency responses are exploited to help infer the presence of a UXO-sized object amidst clutter. The first section below presents relevant formulations and analytical relations. Basic EMI scattering behavior specific to widely dispersed, well-distributed small items is deduced for defined scenarios and assumptions. The role of clutter orientation distributions is analyzed, and specific power laws are derived for the dependence of clutter signals on antenna elevation. Scatterer discrimination processing formulations are brought to bear that include statistical parameters derived from clutter data, for sparse clutter distributions. The next subsection shows

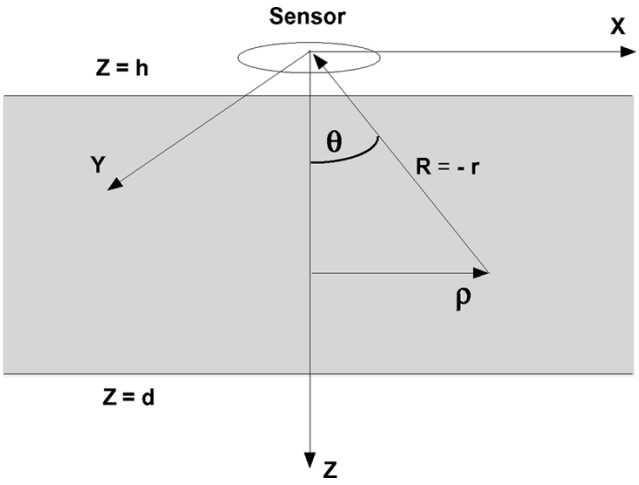


Fig. 3. Sensor resides at the origin, above the ground surface. A clutter layer extends from $Z = h$ to $Z = d$.

tests of the theory against measurements, followed by a section with applications. The latter includes identification of signal patterns from layers of finite thickness; possible routes through the screening problem; the behavior of clutter statistics from sparse distributions as the sensor elevation changes; and evaluation of processing that exploits these clutter statistics patterns, relative to simple least squares treatments.

## II. Formulations and Analytical Relations

### A. Overall Scenario, Assumptions, and Basic Relations

Assume that an EMI sensor resides at the origin of an $(x, y, z)$ coordinate system, with $z$ positive downward, into the ground (Fig. 3). A clutter layer begins at $z = h$, which may or may not coincide with the surface of the ground. As noted above, because currents in the metallic scatterers are approximately nine orders of magnitude greater than those in the soil and only a small volume of soil is typically illuminated in any case, we may assume that the scatterers dominate the received fields. Similarly, the currents in the transmitter are very much greater than any that can be induced in the ground. Altogether then, we assume that the ground itself is effectively transparent to the sensor, producing neither significant scattered fields nor significant alteration of primary field.

In terms of its scattering behavior, when each small metallic clutter object is subjected to the primary (transmitted) magnetic field $\mathbf{H}^{\mathrm{PR}}$ $(A/m)$, it behaves like an anisotropic magnetic dipole with induced magnetic dipole moment $\mathbf{m}$ $(A\ m^2)$. For the $i$th object located at $\mathbf{r}_i$ with magnetic polarizability matrix $\mathbf{M}_i$ $(m^3)$

$$\mathbf{m_i} = \mathbf{M_i} \cdot \mathbf{H}^{\mathrm{ex}}(\mathbf{r_i}) \tag{1}$$

where $\mathbf{H}^{\mathrm{ex}}$ is the total excitation field acting on the $i$th object. The scattered magnetic field $\mathbf{H}_i^s$ from the $i$th object measured at the sensor location $\mathbf{r}_o$ (here, the origin) is [13]

$$\mathbf{H}_i^s(\mathbf{r}_o) = \frac{3\hat{\mathbf{R}}_{io}\hat{\mathbf{R}}_{io} - \mathbf{I}}{4\pi R_{io}^3} \cdot \mathbf{M}_i \cdot \mathbf{H}_i^{\mathrm{ex}} \tag{2}$$

where

$$\mathbf{R}_{io} = \mathbf{r}_o - \mathbf{r}_i \quad R_{io} = |\mathbf{R}_{io}| \quad \hat{\mathbf{R}}_{io} = \frac{\mathbf{R}_{io}}{R_{io}}. \tag{3}$$

Most EMI sensors transmit from horizontal loop antennas. A cylindrical $(\rho, z, \phi)$ coordinate system is often most suitable for expressing the primary field; and a magnetic dipole is a good representative source for testing basic sensitivities, when the sensor loop is small relative to the scale of observation. For use in the expressions below, in cylindrical coordinates the primary field transmitted by an infinitesimal dipole antenna is

$$\mathbf{H}^{\mathrm{PR}} = H_o \left[ \hat{\rho} \frac{3\rho z}{4\pi R^5} + \hat{\mathbf{z}} \frac{2z^2 - \rho^2}{4\pi R^5} \right] \tag{4}$$

where $R = \sqrt{\rho^2 + z^2}$ is the distance from the location of the dipole and $H_o$ is a constant $(A\ m^2)$. For some very large loop transmitters, as are now being considered for EMI sensing of UXO [3], the primary field is uniform at the scale of the geometry in Fig. 3 and only $H_z^{\mathrm{PR}}$ is present.

In some examples pursued by Braunisch *et al.* [14], EMI coupling between members of an array of spherical scatterers is shown to have a negligible effect on the scattered field. Overall, for a small spherical particle $\mathbf{M} = \beta\mathbf{I}$, where $\mathbf{I}$ is the identity matrix and by convention $\beta$ is expressed in the frequency domain as $q[M - iN]$, where $i$ is the square root of $-1$. The normalized, frequency dependent real (in-phase) and imaginary (phase quadrature) parts of the impulse response are expressed by the real valued functions $M(f)$ and $N(f)$, respectively, and $|M - iN| \leq 2$. The overall, frequency-independent magnitude of the polarizability enters through $q$, which for a sphere is $2\pi a^3$, where $a$ is the radius. Insertion of this information into the relations above means that the scattered field from an individual particle falls off as $\sim (a/R)^3$. While the magnitude of the scattered field is $\sim |\mathbf{H}^{\mathrm{PR}}|$ on the particle surface $(R = a)$, it declines by about an order of magnitude at a distance of one radius from the surface $(R \sim 2a)$, and by about two orders of magnitude at one diameter from the surface $(R \sim 3a)$. Based on these considerations, coupling between the clutter items is normally a secondary or negligible effect.

In an exception to this, some recent work has shown significant interaction effects when magnetically permeable objects are separated by distances smaller than their characteristic dimensions [15], [16]. In this case

$$\begin{aligned} \mathbf{H}_i^{\mathrm{ex}} &= \mathbf{H}^{\mathrm{PR}}(\mathbf{r}_i) + \sum_{j \neq i} \mathbf{H}_{ji}^s(\mathbf{r}_i) \\ &= \mathbf{H}^{\mathrm{PR}}(\mathbf{r}_i) + \sum_{j \neq i} \frac{3\hat{\mathbf{R}}_{ji}\hat{\mathbf{R}}_{ji} - \mathbf{I}}{4\pi R_{ji}^3} \cdot \mathbf{M}_j \cdot \mathbf{H}_j^{\mathrm{ex}} \end{aligned} \tag{5}$$

where $R_{ij}$ is the distance between the $i$th and $j$th particles and the summation term represents the action of surrounding particles on the $i$th object [14]. If the primary field is uniform and fixed, then all factors in (5) remain fixed as the observation distance (sensor's $h$) increases. The concomitant decline in the measured response will depend on $h$ only through $R$ as it appears explicitly in (2), for each $i$th particle. For a dipole antenna, the spatially nonuniform excitation field on the $i$th object

and its neighbors declines as $h$ increases. However, the discussion above reveals that the $i$th object will only be influenced by its very nearest neighbors. Thus, the distance of the sensor from the cluster consisting of particle $i$ and its nearest neighbors is $\sim R_{io}$. Both the direct excitation of the $i$th object through $\mathbf{H}^{\mathrm{PR}}(\mathbf{r}_i)$ and its indirect excitation by the action of $\mathbf{H}_j^{\mathrm{ex}}$ on its neighbors will be essentially the same function of $R_{io}$. Otherwise put, because the arrangement of the particles remains fixed as the antenna recedes, both the strength of their direct stimulation and of their interaction will fade by the same factor. That is, as the particle always responds in the same way in connection with its neighbors, its effective polarizability becomes some $\beta_i'$, slightly altered from the value $\beta_i$ that applies to it in isolation. Particularly because the details of the clutter items are typically unknown, we are concerned here primarily with patterns of response from the clutter, e.g., pattern of $h$ dependency, and not on prediction of precise magnitudes at some particular observation point. It is not important whether we are dealing with $\beta_i$ or $\beta_i'$. For our purposes, then, we may generally proceed as if coupling were insignificant, i.e., as if $\mathbf{H}_i^{\mathrm{ex}}$ in (2) were simply $\mathbf{H}_i^{\mathrm{PR}}$, noting that any (rare) effect of coupling is in principle accounted for by adjustments of the effective values within $\mathbf{M}$. None of this alters the general response patterns in which we are interested.

Subject to these understandings, the response to $\mathbf{H}^{\mathrm{PR}}$ from many widely distributed clutter particles can be written as

$$\mathbf{H}^s = \int dV\, p(z) \frac{3\hat{\mathbf{R}}\hat{\mathbf{R}} - \mathbf{I}}{4\pi R^3} \cdot \mathbf{M}(\mathbf{r}) \cdot \mathbf{H}^{\mathrm{PR}}(\mathbf{r}) \qquad (6)$$

where $\hat{\mathbf{R}}$ is now the vector between each $dV$ and the observation point (origin), and the density function $p(z)$ specifies the spatial distribution of the clutter particles as a function of depth. The following two general kinds of clutter distributions will be distinguished for treatment here.

1) Well-distributed, dense clutter, in which $p(z)$ is assumed (statistically) uniform in any horizontal plane, and every $dV$ contains a large sample of particles. $\mathbf{M}$ is construed as a continuous function of $\mathbf{r}$, though its value may be a random variable, e.g., containing particle orientation distributions. The only (potentially) random variable is $\mathbf{M}$.
2) Sparse distributions, in which $\mathbf{M}(\mathbf{r}) = 0$ for most $\mathbf{r}$ and may otherwise be regarded as a delta function at some finite collection of points. Particle positions as well as their characteristics may be random variables.

The second case will be treated separately below via Monte Carlo simulations. In the analytical formulation we concentrate on the first case, considering two particle density distributions explicitly

$$p(z) = \left\{ \begin{array}{ll} 0, & z < h, z > d \\ n_v, & d \geq z \geq h \end{array} \right\}, \quad \text{volume layer}$$
$$p(z) = n_s \delta(z - h), \quad \text{surface layer} \qquad (7)$$

where $n_v$ and $n_s$ are the number of scatterers per unit volume or per unit surface area, respectively. Note that the statistical properties of $\mathbf{M}$ are not a function of $\mathbf{r}$ beyond what is specified in the density distribution $p(z)$. Combinations of statistically different classes of clutter items may still be treated by superposition.

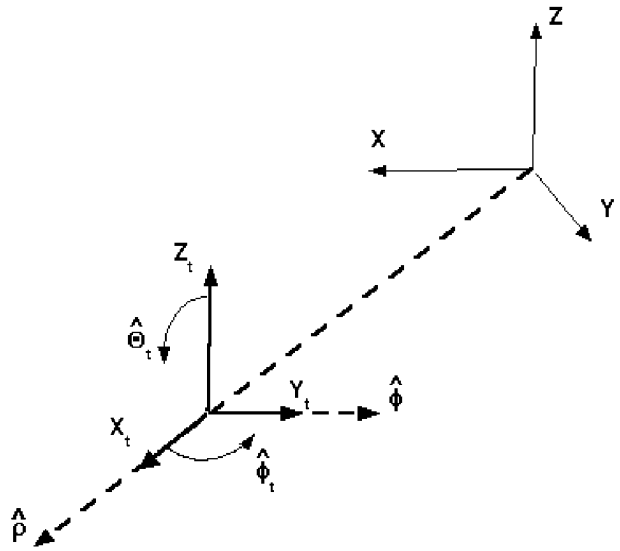


Fig. 4. Local scatterer axes $(x_t, y_t, z_t)$ and associated rotation angles, in relation to the global system.

One can formulate a volumetric $p(z)$ that converges to the one above for a surface layer in effect by constructing a form that produces limitless particle density as the layer thickness goes to zero. While this unifies the treatment mathematically, we have opted here to retain expressions in which the forms of the distributions and the particle density parameter remain separate, and different density measures (per unit volume, per unit area) apply over the domains with different dimensions.

### *B. Orientation Distributions*

Under the conditions and assumptions outlined in the previous section, we proceed with $\mathbf{M}$ expressed as a diagonal eigenvalue matrix, diag $\{\beta_1, \beta_2, \beta_3\}$. This implies a view aligned with the particles' principal scattering axes, which for simple shapes coincides with principal geometrical axes. This suffices for our purposes here, in that random combinations of different $\beta_i$ will produce resultant dipole moments in arbitrary directions. As representative anisotropic objects, we will only consider bodies of revolution (BOR). The two transverse eigenvalues $\beta_2$ and $\beta_3$ are equal, denoted hereafter $\beta_b$, and $\beta_1$ equals the polarizability $\beta_a$ along the principal axis ("axial" polarizability). The orientation of each scatterer is expressed relative to a local coordinate system $(x_t, y_t, z_t)$ with origin at the centroid of the clutter item, where the $z_t$ axis is aligned with the global $z$ axis and $x_t$ is aligned with the global cylindrical $\rho$ axis (Fig. 4). The axis of the scatterer points in some direction $\hat{\mathbf{a}}$, the orientation of which is expressed in terms of local polar and azimuthal angles and their associated unit basis vectors, $\hat{\boldsymbol{\theta}}_t$ and $\hat{\boldsymbol{\phi}}_t$.

In terms of these quantities

$$\mathbf{m} = \beta_a \hat{\mathbf{a}} H_a^{\mathrm{PR}} + \beta_b \hat{\boldsymbol{\theta}}_t H_{\theta_t}^{\mathrm{PR}} + \beta_b \hat{\boldsymbol{\phi}}_t H_{\phi_t}^{\mathrm{PR}} \qquad (8)$$

where local and global coordinate directions are linked by

$$\hat{\mathbf{a}} = \hat{\mathbf{z}} \cos\theta_t + \hat{\boldsymbol{\rho}} \sin\theta_t \cos\phi_t + \hat{\boldsymbol{\phi}} \sin\theta_t \sin\phi_t$$
$$\hat{\boldsymbol{\theta}}_t = \hat{\mathbf{z}} \sin(-\theta_t) + \hat{\boldsymbol{\rho}} \cos\theta_t \cos\phi_t + \hat{\boldsymbol{\phi}} \cos\theta_t \sin\phi_t$$
$$\hat{\boldsymbol{\phi}}_t = \hat{\boldsymbol{\rho}} \sin(-\phi_t) + \hat{\boldsymbol{\phi}} \cos\phi_t \qquad (9)$$

TABLE I

| | |
|---|---|
| Vertically and horizontally omni-directional | $\langle F_z \rangle = \frac{1}{2}[\beta_a + \beta_b] H_z^{PR}$, $\langle F_\rho \rangle = \frac{1}{4}[\beta_a + 3\beta_b] H_\rho^{PR}$ |
| Vertical | $\langle F_z \rangle = \beta_a H_z^{PR}$, $\langle F_\rho \rangle = \beta_b H_\rho^{PR}$ |
| Omni-directional within horizontal layer | $\langle F_z \rangle = \beta_b H_z^{PR}$, $\langle F_\rho \rangle = \frac{1}{2}[\beta_a + \beta_b] H_\rho^{PR}$ |
| Radially oriented within horizontal layer | $\langle F_z \rangle = \beta_b H_z^{PR}$, $\langle F_\rho \rangle = \beta_a H_\rho^{PR}$ |
| Uni-directional horizontal layer | $\langle F_z \rangle = \beta_b H_z^{PR}$, $\langle F_\rho \rangle = \left[\beta_a \cos^2\phi + \beta_b \sin^2\phi\right] H_\rho^{PR}$ |

so that

$$\begin{aligned} H_a^{\mathrm{PR}} &= H_z^{\mathrm{PR}} \cos\theta_t + H_\rho^{\mathrm{PR}} \sin\theta_t \cos\phi_t \\ H_{\theta_t}^{\mathrm{PR}} &= H_z^{\mathrm{PR}} \sin(-\theta_t) + H_\rho^{\mathrm{PR}} \cos\theta_t \cos\phi_t \\ H_{\phi_t}^{\mathrm{PR}} &= H_\rho^{\mathrm{PR}} \sin(-\phi_t). \end{aligned} \tag{10}$$

To preserve sign consistency between the local coordinates and the global sign of $\mathbf{m}$, we consider that $0 \le \theta_t \le \pi/2, 0 \le \phi_t \le 2\pi$. This describes every possible scatterer orientation, given the symmetries of the BOR particles.

In general, the clutter items are randomly oriented according to some distribution $P(\theta_t, \phi_t) = P_\theta(\theta_t) P_\phi(\phi_t)$. Denoting the average of a function $F$ as $\langle F \rangle$

$$\langle F \rangle \equiv \int_0^{\pi/2} d\theta_t \int_0^{2\pi} d\phi_t F(\theta_t, \phi_t) P(\theta_t, \phi_t) \tag{11}$$

one obtains the average or resultant $\mathbf{H}^s$ from (6) and the relations above simply as

$$\langle \mathbf{H}^s \rangle = \int dV p(z) \frac{3\hat{\mathbf{R}}\hat{\mathbf{R}} - \mathbf{I}}{4\pi R^3} \cdot \langle \mathbf{m} \rangle. \tag{12}$$

In typical field practice only $H_z$ is measured, for which the relations above produce

$$\begin{aligned} \langle H_z^s \rangle &= \int dV \frac{p(z)}{4\pi R^3} \{(3\cos^2\theta - 1)\langle F_z \rangle + 3\cos\theta \sin\theta \langle F_\rho \rangle\} \\ &= \int_{z=h}^{d} dz\, p(z) \int_S dS \frac{1}{4\pi R^3} \{(3\cos^2\theta - 1)\langle F_z \rangle \\ &\qquad + 3\cos\theta \sin\theta \langle F_\rho \rangle\} \end{aligned} \tag{13}$$

where

$$\begin{aligned} F_z &= \beta_a \left[H_z^{\mathrm{PR}} \cos^2\theta_t + H_\rho^{\mathrm{PR}} \cos\theta_t \sin\theta_t \cos\phi_t\right] \\ &\quad + \beta_b \left[H_z^{\mathrm{PR}} \sin^2\theta_t - H_\rho^{\mathrm{PR}} \cos\theta_t \sin\theta_t \cos\phi_t\right] \end{aligned} \tag{14}$$

$$\begin{aligned} F_\rho &= \beta_a \left[H_z^{\mathrm{PR}} \cos\theta_t \sin\theta_t \cos\phi_t + H_\rho^{\mathrm{PR}} \sin^2\theta_t \cos^2\phi_t\right] \\ &\quad + \beta_b \left[H_z^{\mathrm{PR}} \cos\theta_t \sin(-\theta_t) \cos\phi_t \right. \\ &\qquad \left. + H_\rho^{\mathrm{PR}} (\cos^2\theta_t \cos^2\phi_t + \sin^2\phi_t)\right]. \end{aligned} \tag{15}$$

Illustrative examples of $P_\theta(\theta_t)$ and $P_\phi(\phi_t)$ are

$$P_\theta(\theta_t) = \left\{ \begin{array}{c} \frac{2}{\pi}, \text{omnidirectional (uniform) over polar angle} \\ \delta(\theta_t), \text{vertical} \\ \delta(\theta_t - \pi/2), \text{horizontal} \end{array} \right\} \tag{16}$$

and

$$P_\phi(\phi_t) = \left\{ \begin{array}{c} \frac{1}{2\pi}, \text{uniform over azimuthal angle} \\ \frac{1}{2}\{\delta(\phi_t) + \delta(\phi_t - \pi)\}, \text{radial}(\hat{\boldsymbol{\rho}}) \\ \frac{1}{2}\{\delta(\phi_t + \phi) + \delta(\phi_t + \phi - \pi)\}, \text{unidirectional}(\hat{\mathbf{x}}) \end{array} \right\}. \tag{17}$$

Execution of the averaging operations in (13) based on (16) and (17) produces Table I.

### C. Effect of Sensor Elevation $h$

All the results in Table I above imply the solution for spherical clutter particles, for which $\beta_a = \beta_b = \beta$

$$\begin{aligned} \langle H_z^s \rangle = \beta \int_{z=h}^{d} dz\, p(z) \int_S dS \frac{1}{4\pi R^3} \\ - \left\{(3\cos^2\theta - 1) H_z^{\mathrm{PR}} + 3\cos\theta \sin\theta H_\rho^{\mathrm{PR}}\right\}. \end{aligned} \tag{18}$$

As pursued more specifically below, the different orientation distributions for anisotropic clutter items, as expressed through (13), simply weight the participation of $H_z^{\mathrm{PR}}$ and $H_\rho^{\mathrm{PR}}$ differently relative to the expressions in (18). In particular, in each case the $h$ dependence of the terms on the right in (13) and (18) will be the same; therefore we will study the consequences of the latter, simpler equation explicitly.

To carry out the integrations in (18) note that, over each horizontal surface $S$, $z$ is constant, $R = z/\cos(\theta)$, and $dS = d\rho\rho d\phi$, where $\rho = z\tan(\theta)$, and $d\rho = z d\theta/\cos^2(\theta)$. Thus, the integration over S becomes an integration over $\theta$ and $\phi$. If the primary fields from our loop antennas are axisymmetric, then all the values of $\langle F_z \rangle$ and are constant over the integration with respect to $\phi$ except in the case of the unidirectional horizontal layer. However the latter integrates over $\phi$ to produce the same result as for the omnidirectional horizontal layer, for which $\langle F_z \rangle$ and $\langle F_\rho \rangle$ are constant with respect to $\phi$. This all emphasizes what is apparent if one considers the implications of (12) directly: Clutter orientation distributions that are independent of position simply imply how much the different axes of the scatterers interact with each primary field component. This in turn will affect the overall magnitude of response as well as the magnitude of response due to scatterers at any given position, as the sensor is raised or lowered so that $H_z^{\mathrm{PR}}$ and $H_\rho^{\mathrm{PR}}$ and their relations change. However, even for nonuniform primary fields, the orientation distributions do not affect the dependency of $\langle H_z^s \rangle$ on sensor elevation, beyond a scaling factor. Thus, we will investigate the basic sensitivities of $\langle H_z^s \rangle$ to $h$ using (18), in terms of $H_z^s$, with the understanding the results may simply be scaled

uniformly for anisotropic clutter items and averages over their orientation distributions.

Analytically, we consider below two specific types of excitation, namely a uniform primary field $\mathbf{H}^{\mathrm{PR}}(H_z^{\mathrm{PR}}=1, H_\rho^{\mathrm{PR}}=0)$ and a magnetic dipole excitation field (4). In practice, a small number of infinitesimal magnetic dipoles is often a good fundamental representation of the kinds of sources in existing instrumentation, provided the scatterers are a sufficient distance away (see measurement tests below). For a uniform primary field (18) becomes

$$H_z^s = \frac{\beta}{2}\int_{z=h}^{d} dz\, p(z) \int_{\rho=0}^{\infty} \rho d\rho \frac{3\cos^2(\theta)-1}{(z/\cos(\theta))^3} \tag{19}$$

$$H_z^s = \frac{\beta}{2}\int_{z=h}^{d} dz \frac{p(z)}{z} \int_{\theta=0}^{\pi/2} d\theta \sin(\theta)(3\cos^2(\theta)-1) = 0. \tag{20}$$

Thus, when subjected to a uniform primary field, a distribution of particles that is perfectly uniform statistically will produce null response in a localized receiver. This is true for both of the $p(z)$ distributions in (3); that is, it is the zero value of the integration with respect to $\theta$ at each Z value, that nullifies the entire integration.

This suggests that a very large excitation loop, as required for a uniform primary field, will minimize the response of widespread clutter relative to an object of interest, as long as the clutter is well distributed at least over the footprint of the receiver. It also suggests the main limitation of this result. Namely, the clutter may not be sufficiently uniform in its horizontal distribution for this result to hold, i.e., the integration with respect to $\theta$ for any actual realization may produce some nonzero value, say $V$. Then we obtain

$$H_z^s = V\frac{n_s\beta}{2}\frac{1}{h}, \quad \text{surface layer} \tag{21}$$

$$H_z^s = V\frac{n_v\beta}{2}\ell n\left(\frac{d}{h}\right), \quad \text{volume layer.} \tag{22}$$

Thus when the clutter is spread entirely over a surface, any effect on the received signal will decline only in inverse proportion to the height of the antenna. When the clutter is spread over a volume layer, the signal will be inversely proportional to the log of antenna height, scaled by the depth to which the clutter is found. As indicated above, (22) does not converge to (21) as $d \to h$ only because, in the former, we assume that the scatterers are volumetrically distributed with $n_v$ per unit volume, so that a layer of zero thickness contains zero scatterers. Convergence between the two forms can be achieved by adjusting $n_v$ as thinner layers are treated, so that a finite mass of particles is always present. In any case, as we demonstrate below using these expressions, the pattern of the scattering behavior from the volume layer does indeed tend toward that of an infinitesimally thin layer as $d \to h$. Note that the signal from the volume layer declines as the antenna is raised because, while both $d$ and $h$ increase, $d/h \to 1$. Relative to all other cases to be considered, this decline is very slow.

When the primary field can be approximated by that emitted by an infinitesimal magnetic dipole then, with the various geometrical relations above, all integrations can be carried out by elementary methods, yielding

$$H_z^s = \frac{11\beta}{140}\int_{z=h}^{d} dz \frac{p(z)}{z^4} \tag{23}$$

so that

$$H_z^s = \frac{11\beta n_s}{140}\frac{1}{h^4}, \quad \text{surface layer}$$

$$H_z^s = \frac{11\beta n_v}{420}\left[\frac{1}{h^3}-\frac{1}{d^3}\right], \quad \text{volume layer.} \tag{24}$$

In these cases, as the sensor is elevated, the signal received from the clutter declines much more rapidly than for the uniform primary field, as does the signal from a larger object of interest. For the infinite halfspace, $(d \to \infty)$, note that the volume layer response has the same $1/h^3$ dependency as the analytical solution for a halfspace consisting of a continuous permeable medium [17].

Specialized for the primary field produced by a real sensor, the relations above will be tested against data from manual randomizations of the dense, relatively well-distributed clutter in Fig. 1. These same clutter distributions will then be used to evaluate strategies for dealing with the screening problem.

### *D. Including Clutter Signal Statistics in Inversion for Sparse Distributions*

The items in Fig. 2 provide a reasonably realistic representation of sparse near-surface clutter that might obscure or screen the response of a deeper, larger object of interest. In lab tests, measurements over grids of points on horizontal planes produced the sampling from which response statistics were derived. These show that such sparse, diverse clutter fails to provide recognizable statistical distributions of response that would permit continuous mathematical expression. Nevertheless, a mean $(\mu_d)$ and standard deviation $(\sigma_d)$ of the data can always be obtained. As a heuristic approach, we will perform discrimination processing of signals contaminated by this clutter using formulations that include statistical parameters. Approaches based on ideal statistical distributions have been used elsewhere in UXO discrimination exercises, with encouraging results [18]–[20]. Our data (and that in most of the nominally statistical treatments in the literature) do in fact not meet rigorous preconditions of the underlying theory. Here we simply refer to formulations based on ideal statistical theory for potentially useful guidance on weighting, centering (penalizing), and regularization of the least squares optimization. Results from our statistically weighted least squares (SWLS) approach [25] are compared with the discrimination performance obtained using simple least squares (SLS) processing. The latter contains no regularization or penalty functions, and no (i.e., unitary) weighting of sum of squares.

In terms of our data here, the SLS calculations proceed simply by minimizing the objective function $\Phi = \sum_{i=1}^{N_o}\sum_{n=1}^{N_f}\left|H_d - H_m\right|^2$ over the total number of observation points and frequencies ($N_o$ and $N_f$, respectively). $H_m(H_d)$ is the modeled (measured) magnetic field response in the $Z$ direction, at a particular frequency and observation position (i.e., $H_z(\mathbf{r}_i, f_n)$), for any particular (assumed) set of the scatterer's parameters. Assuming that we are seeking some object

parameters $a$ and $b$, the SWLS approach entails minimizing the objective function

$$\Phi(a,b) = \{H_d - H_m\}^T \cdot [W] \cdot \{H_d - H_m\} + \left(\frac{a-a_o}{s_a}\right)^2 + \left(\frac{b-b_o}{s_b}\right)^2 \quad (25)$$

where the appropriate ($h$ dependent) clutter mean has been subtracted from $H_d$. This is discussed further below. The diagonal matrix $[W]$ of weights in the summation consists of $1/\sigma_{d,j}^2$ for each $j$th data point. Assuming that we are seeking two parameters $a$ and $b$, the last two terms are penalty functions that serve to drive the optimization toward a region of reasonable values. If some prior knowledge of target statistics is available, $(a_o, b_o)$ and $(s_a, s_b)$ may be means and standard deviations, respectively, inherent in manufacture processes or environmental influences on the objects sought. In the examples pursued here, the $(a_o, b_o)$ simply imply that we know what class of objects we are looking for, for which certain regions of search are sensible, and the weight of the penalty terms relative to the summation term is controlled by $(s_a, s_b)$.

If the true probabilities for each of the object's dimensions $a$ and $b$ were ideal Gaussian distributions and at the same time the distributions for $H_d$ were as well, and if further the correlation between data samples were negligible, then minimizing $\Phi(a,b)$ would constitute a Bayesian approach. However, none of these assumptions is even remotely accurate. For this reason we deem the formulation of $\Phi$ "Bayesian inspired," but only in the sense that we look toward the ideal statistical for guidance in selecting potentially beneficial $[W], (a_o, b_o)$, and $(s_a, s_b)$. At root, each variant of our formulation is based on least squares, admitting essentially arbitrary selection of the parameters depending on ulterior considerations, sometimes at variance with the choices implied by the ideal Bayesian forms. For example, if values of signal deviation $\sigma_d$ are essentially flat across all frequencies and measurement points, then using $1/\sigma_{d,j}^2$ for each $j$th diagonal element in $[W]$ may be sensible: It serves to deemphasize weaker signals. However, in other instances $\sigma_{d,j}$ may be proportional to the magnitude of the $j$th data point. Applying $1/\sigma_{d,j}^2$ in $[W]$ then tends to weight both strong and weak data equally, which may well be inappropriate. Further, in practice we are very unlikely to be able to obtain rigorous $\sigma_d$ values for each frequency and measurement position. In the examples here, each $\sigma_d$ value was estimated based on signal variability over an ensemble of positions at a each sensor elevation, i.e., $\sigma_d = \sigma_d(h)$. Thus, the data were segmented for statistical estimation purposes, based on expectations borne of the theory developed above. In other instances we find it beneficial or essential to add a "noise floor" to $\sigma_d$, the value of which may be unrelated to true noise levels. All these observations are only intended to emphasize that the formulation in (25) is fundamentally a least squares approach, with parameter selection inspired by, but by no means truly derived from ideal statistical theory.

## III. Tests Against Measurements

To test the applicability of (18), measurements were made over the two dense surface clutter distributions in Fig. 1 using the GEM-3 sensor. No attempt was made to estimate magnetic polarizability or particle densities, $\beta$ or $n_s$, in part because the correspondence of sensor output units to actual $H$ values is unknown. Rather, patterns were compared by subjecting the theoretical and experimental curves to the normalization produced by matching them at a single point (usually the strongest). Similarly, comparisons to data can be carried out using any convenient single frequency. Fig. 5 illustrates sequences of measurements at different heights over the clutter layer in Fig. 1 (top). Except for a small amount of low-amplitude, high-frequency drift, the same relative signal magnitudes between different heights apply at all frequencies across the band.

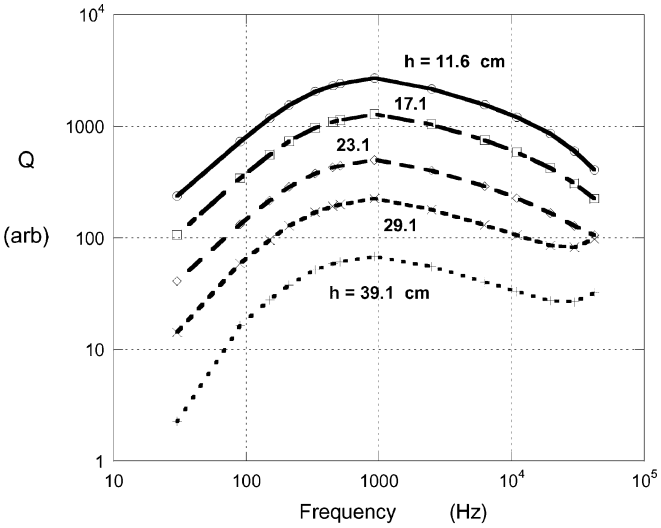


Fig. 5. GEM-3 quadrature response versus frequency, for different sensor elevations over the clutter layer in Fig. 1, top.

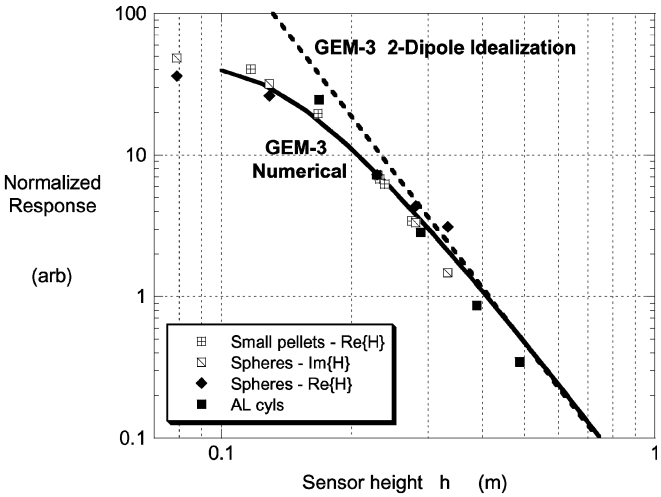


Fig. 6. Markers: GEM-3 response magnitude versus antenna height above a dense surface distribution of randomly dispersed small pellets (30 Hz) and of the steel spheres (11 kHz) and the AL cylinders in Fig. 1 (930 Hz). The dashed line shows the response pattern predicted by a two-dipole idealization of the GEM-3, and the solid line indicates results for a detailed numerical modeling of the instrument's primary field.

Fig. 6, shows results pertaining to the frequency of the quadrature (Q) peak for the short aluminum cylinders and to the indicated frequencies for the other clutter layers. The numerical result is obtained from (18) by simple quadrature, using numerical expressions for the GEM-3 primary field based on the Biot–Savart law [13]. The analytical result (straight dashed line) is obtained when the GEM-3 is modeled using (24)

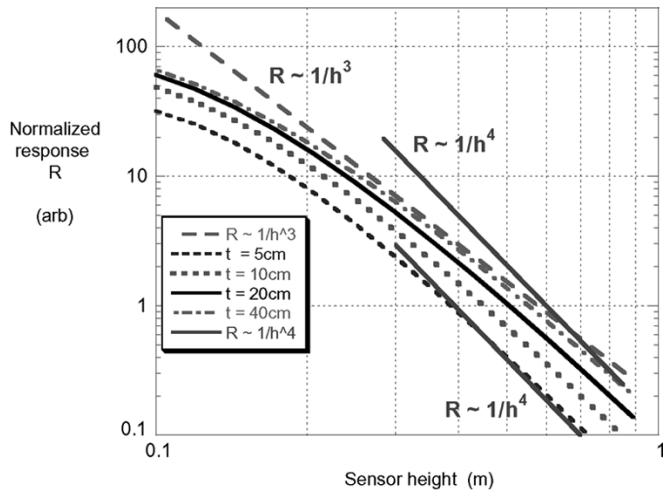


Fig. 7. Calculated GEM-3 responses $R$ from well-distributed clutter in layers of various thicknesses $t$, compared to a line with log-log slope of $-3$ for $R \sim 1/h^3$ and of $-4$ for $R \sim 1/h^4$.

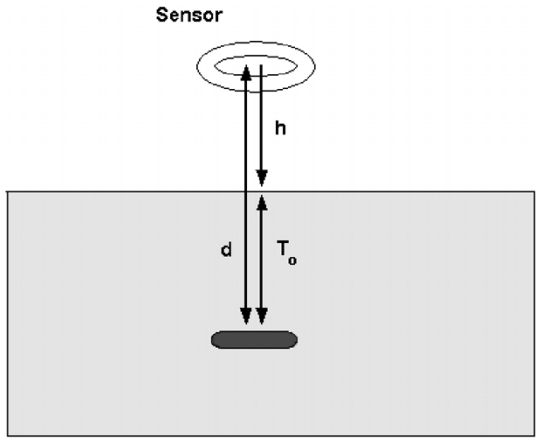


Fig. 8. Setup for analysis of SCR versus sensor height.

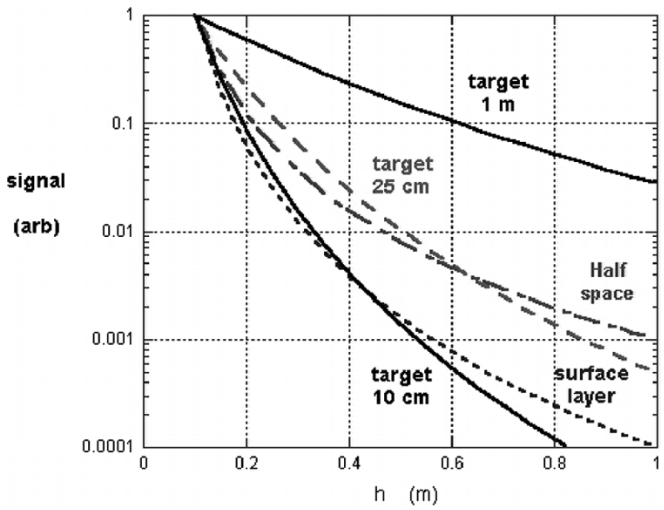


Fig. 9. Received signals from surface and halfspace clutter layers and from a discrete object at indicated depths below ground surface, as a function of antenna height $h$, when the transmitter is a magnetic dipole.

for two oppositely directed infinitesimal dipoles, representing the two mutually opposed, finite transmitter loops. This dipole representation of the GEM-3 is simple to apply and is reasonably accurate, on this log-log scale, for antenna elevations above about 20 or 30 cm. In general, the GEM-3 field can be represented arbitrarily accurately and very efficiently with a collection of dipoles or fictitious magnetic charges, usually modest in number [21], [22]. Particularly for calculating values of scalar potential, as opposed to magnetic field, the dipole formulations are much faster than the Biot-Savart integrations. This is significant for inversion processing. No explicit measures were taken to include orientation distribution effects for the AL cylinders; rather, as discussed above, that is accomplished by the normalization. The curve for the calculated GEM-3 response was not used for elevations less than 10 cm, because the primary field is highly nonuniform in that region and the numerical model of the antenna is not accurate there. The evident good agreement between theory and measurement validates the formulation leading to (18). The implication of these results is that, knowing the spatial distribution of clutter statistics, one can represent faithfully the patterns of EMI response produced by clouds of clutter.

## IV. Applications

### A. Layers of Finite Thickness

Equation (24) indicates that a dipole sensor signal from a half space of well-distributed clutter will decay as $\sim 1/h^3$. Fig. 7 shows computed responses from the GEM-3 for layers of different finite thicknesses that are otherwise identical ($\beta n_v = 1$). The primary field values are obtained numerically and in all cases are normalized by the same factor. Thus, the normalization does not alter the relative magnitudes of responses to be expected from different layers. The 40-cm width of the sensor head provides some degree of spatial scale. Overall, increase in layer thickness $t$ by a factor of 8 increases the response by about a factor of 3. With repeated doubling of $t$, the curves clearly converge on a limiting behavior, paralleling the $\sim 1/h^3$ line in the midrange values of $h$. The curves for smaller values of $t$ shift to a steeper slope at higher values of $h$, moving in the direction of the $\sim 1/h^4$ relation that applies to an infinitely thin ("surface") layer. That is, from greater height the thinner layers appear more like surface distributions than the thicker ones. Overall, for the higher values of $h$ for which we expect dipole-like sensor behavior, the pattern for the 40-cm layer resembles that of a half space, the 5- and 10-cm layer patterns tend toward that for a surface distribution, with the 20-cm result in between.

### B. Screening Problem

To explore the effects on object visibility relative to smaller clutter, consider the setup shown in Fig. 8 with a dipole antenna. The object is assumed to respond as a point scatterer with signal decaying as $1/d^6$ while surface and volume layers of well-distributed clutter obey the power laws (24) above. Fig. 9 shows signal strengths from both clutter and object, separately, when all responses are normalized so that they are the same at the initial antenna height (0.1 m). As the antenna is raised from 0.1 to 1 m, the various clutter layer signals decline between about three and four orders of magnitude. How the scatterer's signal behaves relative to this is completely dependent on its depth.

The signal from the shallowest object fades at about the same rate as the surface layer signal. Signals from the intermediate depth object fades in much the same way as the volume layer. However, the most important observation is that the signal from the object at intermediate depth fades much less rapidly than that from the surface layer, and the deepest object's signal fades much less rapidly than that from either of the clutter distributions. While the power law $(1/d^6)$ for the scatterer is more severe than the relations for the clutter $(1/h^3$ or $1/h^4)$, the smaller change in $d$ relative to its initial value more than compensates, at least initially.

These observations can be generalized using the analytical expressions above. The depth of the object below the surface is expressed as $T_o = nh_o$ where $h_o$ is the initial elevation of the sensor above the ground surface. As the antenna is raised, the signal $s$ from the object declines according to

$$\frac{s}{s_o} = \left(\frac{d_o}{\mathrm{d}}\right)^{mt} = \left(\frac{1+n}{h_r+n}\right)^{mt} \tag{26}$$

where $h_r = h/h_o, mt$ is 3 for the uniform primary field, and is 6 for the dipole primary field.

The clutter signal $C$ declines as the antenna is raised according to

$$\frac{C}{C_o} = \left(\frac{1}{h_r}\right)^{mc} \tag{27}$$

where *mc* is 1 for the uniform primary field and a surface layer of clutter; is 3 for the half space of clutter below a dipole primary field; and is 4 for the surface layer of clutter with dipole primary field. Thus, the relative change in signal-to-clutter ratio (SCR) will be given by

$$\frac{\mathrm{SCR}}{\mathrm{SCR}_o} = \left(\frac{1+n}{1+n/h_r}\right)^{mt} h_r^{mc-mt}. \tag{28}$$

As $h_r$ increases, at some point the expression in brackets will cease to change significantly and the SCR will only decline indefinitely with further elevation of the sensor, in proportion to $h_r^{mc-mt}$. However, for the relevant range of about $1 < h_r < 10$, gains in SCR are often seen. Fig. 10 shows how the SCR changes for different relative object depths n. For a uniform primary field, little is accomplished by raising the antenna. For the dipole primary field, elevation helps, more so for deeper objects. Note that there will be a maximum benefit at intermediate $h/h_o$ values for all but the shallowest object depths.

Of course, a real scatterer, sizable compared to the problem dimensions, will not behave as an ideal infinitesimal dipole at a discrete depth. To pursue this and to support the conclusions above, GEM-3 measurements were made with the antenna above the surface clutter layer in Fig. 1 (top). An 18-in long and 3-in diameter steel cylinder was oriented vertically and placed below the surface. Fig. 11 shows the independently normalized quadrature components of the steel spheres and also of the large steel cylinder, when each is alone. This is encouraging from the viewpoint of discrimination in that they show completely contrasting trends, with that for the cylinder falling monotonically with frequency, and that for the spheres generally rising into the higher frequencies. Fig. 12 shows the $Q$ component magnitude measured with the steel cylinder beneath the clutter surface, for different sensor heights above

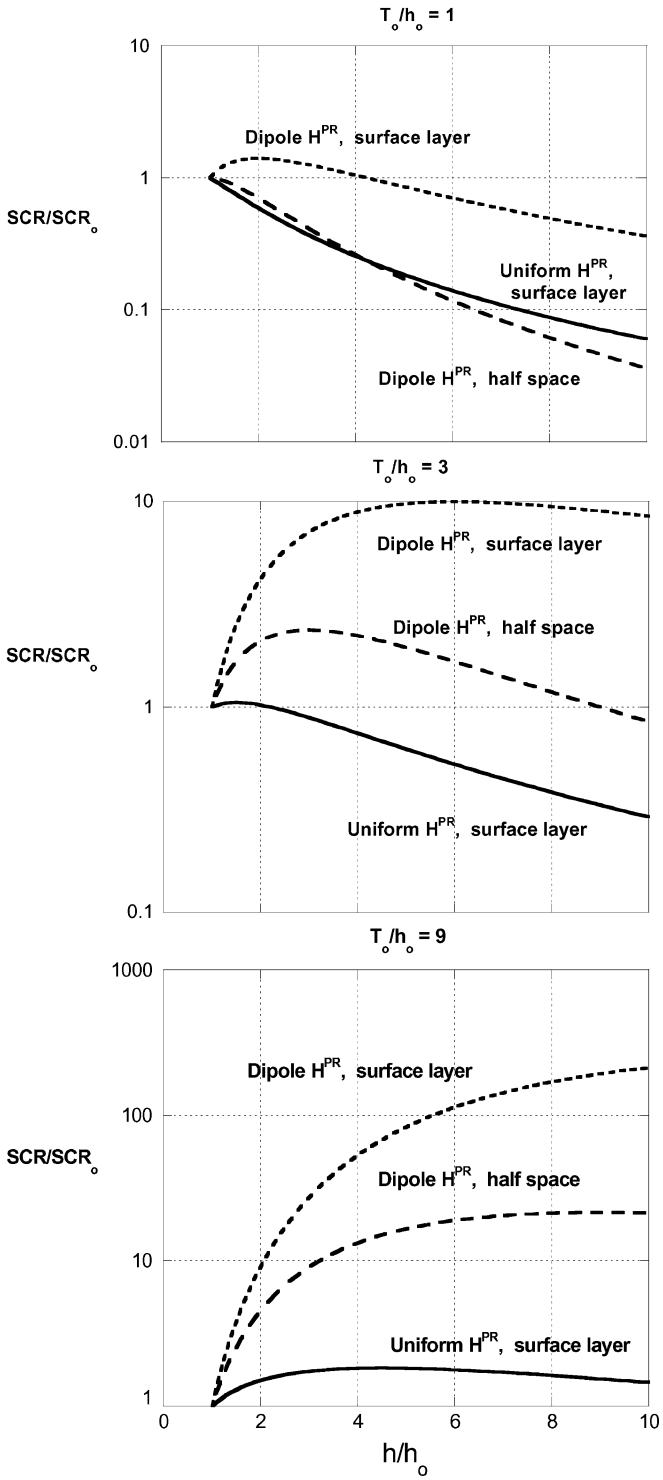


Fig. 10. SCR relative to its value at the initial height $h_o$, as a function of $h/h_o$.

the surface. The figure shows a distinct progression as the antenna is raised. At the lowest elevation $(h_1)$, the $Q$ curve does not resemble the pattern for either target very closely, but is generally more similar to that for the surface clutter, which is proportionally much closer to the antenna. At the maximum height $h_4$ the mix of signals has changed. In particular, as the antenna is raised the cylinder achieves stronger participation, strengthening the lower frequency portion of the curve. Thus, despite the complexity of the GEM-3 primary field and the fact

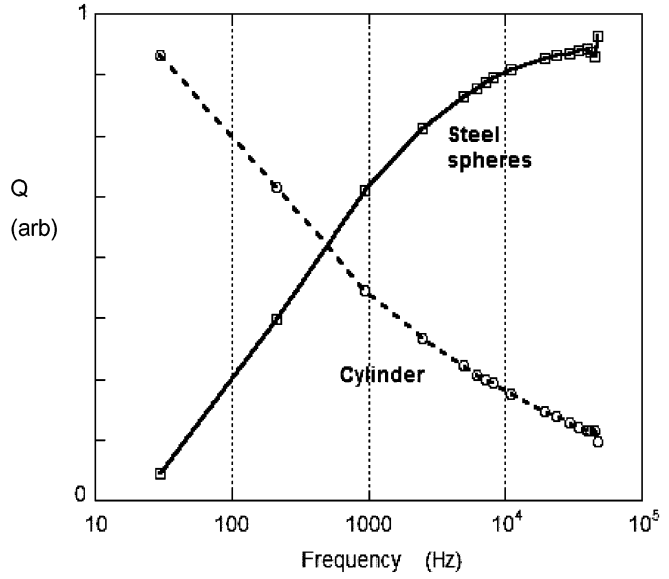


Fig. 11. Semilog plots of independently normalized quadrature components $Q$, measured with the GEM-3, for the surface layer of steel spheres and for the vertical large steel cylinder, each alone.

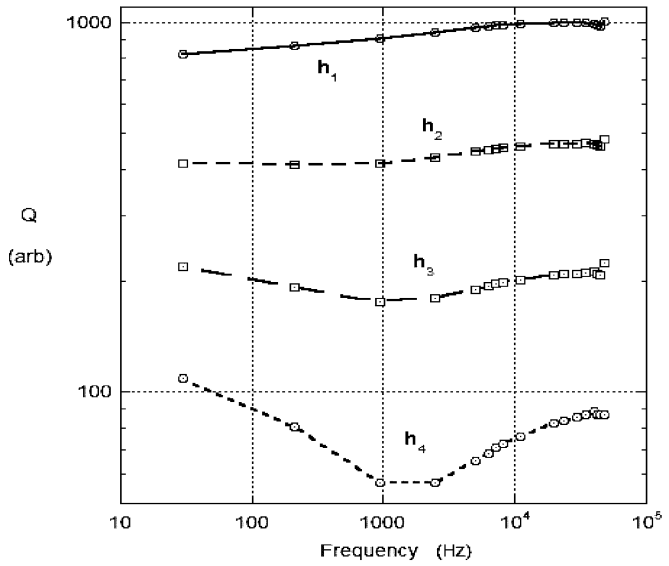


Fig. 12. Log-log plots of quadrature response from randomized surface layer of steel spheres with the large vertical steel cylinder beneath, for successive antenna heights above the surface between $h_1 \sim 18.3$ cm and $h_4 \sim 33.5$ cm.

that the cylinder extends over a large depth range, one sees the kinds of effects predicted on the basis of (28). Raising the antenna has produced a partial segregation of the signals from the two scatterer classes, into different regions of the spectrum.

It is important to note that Fig. 12 contains results that have all been normalized relative to a single reference value, then displayed relative to a log scale in the vertical axis. This is used to emphasize the principal caveat attached to any strategies in which one raises a dipole type antenna, namely, the drop in absolute signal magnitude. Raising the antenna very much will reduce signals to background values, limiting the range of applicability of this approach. In Fig. 12, clutter and target signals decline about one to two orders of magnitude. As indicated in Fig. 6, raising the antenna some tens of centimeters beyond

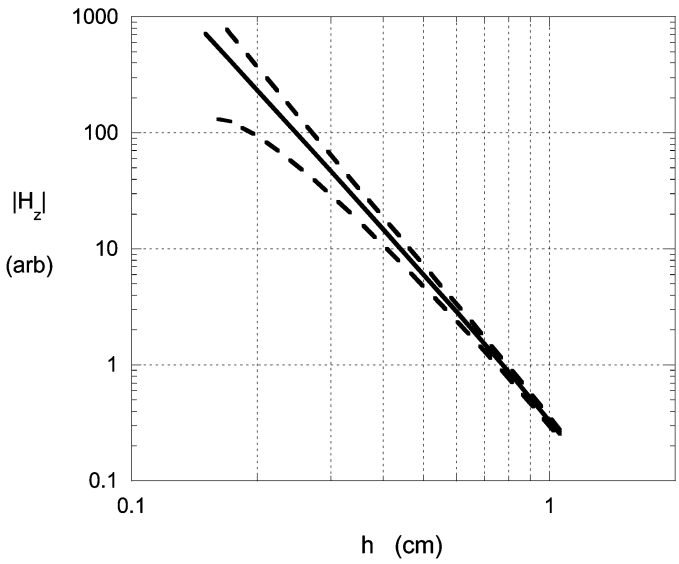


Fig. 13. Simulations of response versus height from randomized 4-m$^2$ surface layers of anisotropic clutter items beneath a dipole source, with $N_p = 100, N_{\min} = 20, \langle Nc \rangle = 26$ and StdDev$\{N_c\} = 3.7$, showing (dashed) envelope of one standard deviation about $\langle |H_z| \rangle$.

the maximum height for the data shown in Fig. 12, but still less than 1 m, would likely reduce signals to the level of background noise.

### *C. Behavior of Signal Statistics Versus Sensor Elevation for Sparse Distributions*

All the cases considered above involved well-distributed clutter. That is, the density of the clutter and similarity of the individual scatterers was such that essentially every horizontal sensor position received about the same response. Otherwise put: each contributing subdomain of cluttered surface could be assumed to produce a fairly close approximation of the average behavior, and variance of the received signal across observation points is small. Now we investigate what is probably a more realistic scenario, namely one in which the clutter items are more various in themselves and are more sparsely distributed. Monte Carlo simulations determine the statistics of response from classes of clutter layers consisting of particles assumed to respond as triaxial point dipoles. A random number generator produces both the positions of the particles as well as their principal polarizabilities $\beta_i$. For the polarizabilities, a flat distribution of magnitudes between 0 and 1 is applied. For the clutter items, $N_p$ particles are spread over 4 m$^2$ and distributions are rejected with fewer than $N_{\min}$ particles within the central square meter, i.e., within the area directly under the observation point. Constrained by $(N_p, N_{\min})$, this process produces some number $N_c$ of particles in the central square meter, differing from the ensemble average $\langle N_c \rangle$ by StdDev$\{N_c\}$. The program runs 1000 cases for each sensor height and records the statistics of the received field, for both dipole and uniform primary fields. Fig. 13 shows the results for the dipole primary field, where the solid line is the ensemble average of scattered $|H_z|$, and the dashed lines indicate one standard deviation above and below the average. As in measurements over the clutter in Fig. 2, shown in a section below, at the lowest antenna position the

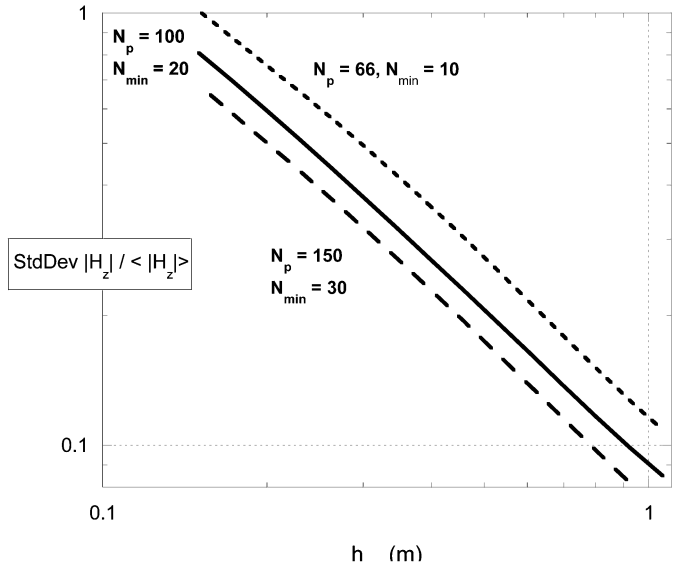


Fig. 14. Percent StdDev of $|H_z|$ is approximately proportional to $1/h$.

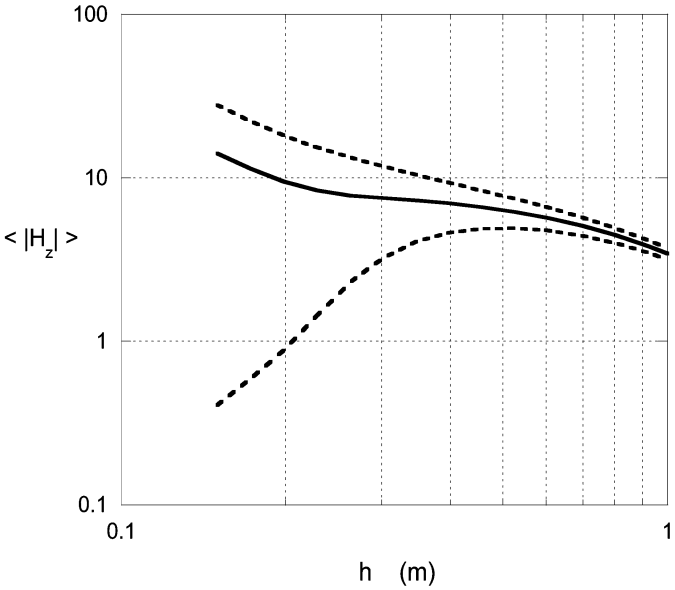


Fig. 15. Average $|H_z|$ for sparse distributions under a uniform primary field, with $N_p = 150, N_{\min} = 30, \langle N_c \rangle = 37$ and StdDev $N_c = 8$.

standard deviation is on the order of 100% of the value of the average. Observations for smaller $N_{\min}$ show that the deviation increases markedly.

Reassuringly, the height dependence of $\langle |H_z| \rangle$ adheres reasonably closely to the $1/h^4$ rule. Perhaps most notable for statistical processing is the relation between StdDev$\{|H_z|\}$ and $\langle |H_z| \rangle$, as a function of $h$ (Fig. 14). The standard deviation declines more rapidly with $h$ than $\langle |H_z| \rangle$, in particular StdDev $\{|H_z|\} \sim 1/h^5$. A uniform $H^{\mathrm{PR}}$ over the same test ensemble produces comparatively little change in $\langle |H_z| \rangle$ as $h$ increases (Fig. 15). This is in line with the results derived analytically for the dense, well-distributed layers, i.e., (19)–(22). Those results indicate that any nonzero value should merely be the residue of imperfect cancellation during the averaging over a finite population, as opposed to a systematically finite value, and on average

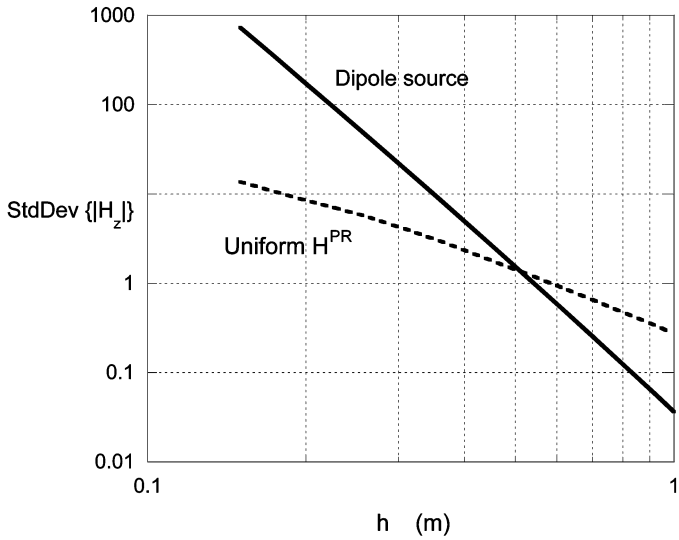


Fig. 16. StdDev$\{|H_z|\rangle$ for the same case as in Fig. 15, but for both dipole source and uniform primary field.

it should decline quite slowly with $h$ (i.e., $\sim 1/h$). The StdDev $\{|H_z|\}$ for the uniform $H^{\mathrm{PR}}$ case also shows commensurately less change with antenna elevation. As in the dipole case, the standard deviation declines an order of magnitude more rapidly than does $\langle |H_z| \rangle$, i.e., roughly proportional to $\sim 1/h^2$ for the uniform primary field as opposed to $\sim 1/h^5$ for the dipole source (Fig. 16).

The preceding addresses the question of how responses for individual realizations ($\sim$ positions on the landscape) compare statistically to the ensemble (field) average. Alternatively, and perhaps more relevant to survey practice, one may query the statistics of signal behavior as a function of height over individual positions (realizations) with respect to the $1/h^4$ power law. That is, for each realization of particle characteristics and arrangements, how closely will the signal follow $\sim A/h^4$ for some $A$, however different any one $A$ may be from that for the ensemble average? This may furnish better guidance on the question of whether it is beneficial or not to change antenna elevation in any given instance. Over a given realization, we only expect some close approximation of the $A/h^4$ for significant sensor elevations, i.e., when a relatively larger number of particles is contributing. Therefore, for each realization in the 1000 Monte Carlo simulations, a SLS best fit $A$ is determined for the $A/h^4$ rule, for $h > 50$ cm. The data in the same realization for all $h$ values $>10$ cm are then compared to those predicted by the resulting $A/h^4$ rule. That is, the signal fade over each realization ($\sim$ location) is compared to a locally derived $1/h^4$ rule, as opposed to one obtained from global ($\sim$ field) averages. Fig. 17 shows the statistical behavior of the deviation of signals from that predicted by the "local" $1/h^4$ rule. While here a linear log-log relation does not appear as in Fig. 14, because the fit was forced for $h > 50$ cm, still the overall patterns in the global and local statistics are similar. Based on the magnitudes in the deviations, Fig. 17 is somewhat more encouraging than Fig. 14, in that the variation from the ideal behavior is somewhat less: One has more reason to believe that the order of magnitude of clutter signals will fade as $1/h^4$ relative to the predominating local values than to some field average.

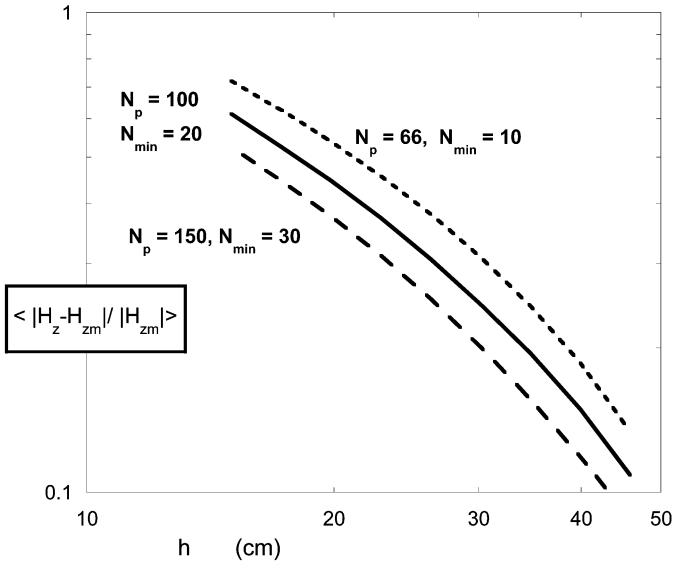


Fig. 17. Average magnitude of deviation of received $H_z$ from the locally modeled value $H_{zm} = A/h^4$ for different clutter densities.

### *D. Implementation of Clutter Statistics in Processing: SWLS Versus SLS*

To explore the utility of the above clutter statistics in UXO discrimination, experiments were performed based on measurements over the clutter layer in Fig. 2. Broadband GEM-3 data were recorded over a $5 \times 5$ grid of positions, with the clutter items rearranged three times for each grid. Each position was at least 10 cm from the next nearest (see position marks in the figure), with an antenna elevation of 10 cm. Mean and standard deviation were calculated over these samples, for each of the 17 frequencies, for both in-phase and quadrature components of response (Fig. 18). A target of interest is represented by a prolate spheroid. We have shown elsewhere that spheroids can sometimes be used effectively to represent the EMI responses of more complicated target geometries [21]–[23]. Modeling a UXO as a prolate spheroid is particularly convenient because an analytical solution can easily be evaluated, at least for high permeability materials, even for realistic sensor primary fields. To match the response of a particular small UXO in either horizontal or nose up position, the spheroid here is assigned minor semiaxis $a_o = 3.8$ cm, major semiaxis $b_o = 18$ cm, electrical conductivity $\sigma = 4 \times 10^6$ S/m, and relative magnetic permeability $\mu_r = 287$ [23]. It is situated nose up at depth $z_o$ below the clutter surface and tilted at 45° relative to vertical. Data for testing alternative inversion approaches at selected SCR values is obtained by assuming that the target is located at some chosen $z_o$, then superposing the recorded GEM-3 clutter signals at each $(\mathbf{r}, f)$, after scaling it to achieve a selected maximum SCR at $h_o$.

In the first set of test cases, the clutter and antenna are fixed and we consider the effects of different possible $z_o$. Using the synthesized, cluttered observations of the target from all spatial positions on the clutter measurement grid, the SLS and SWLS systems invert the data for values of $a$ and $b$. No statistical information is used in the SLS processing. In the SWLS calculations, the (frequency dependent) ensemble value of $\sigma_d$ is used for $\sigma_{d,i}$ at each observation point, and the ensemble

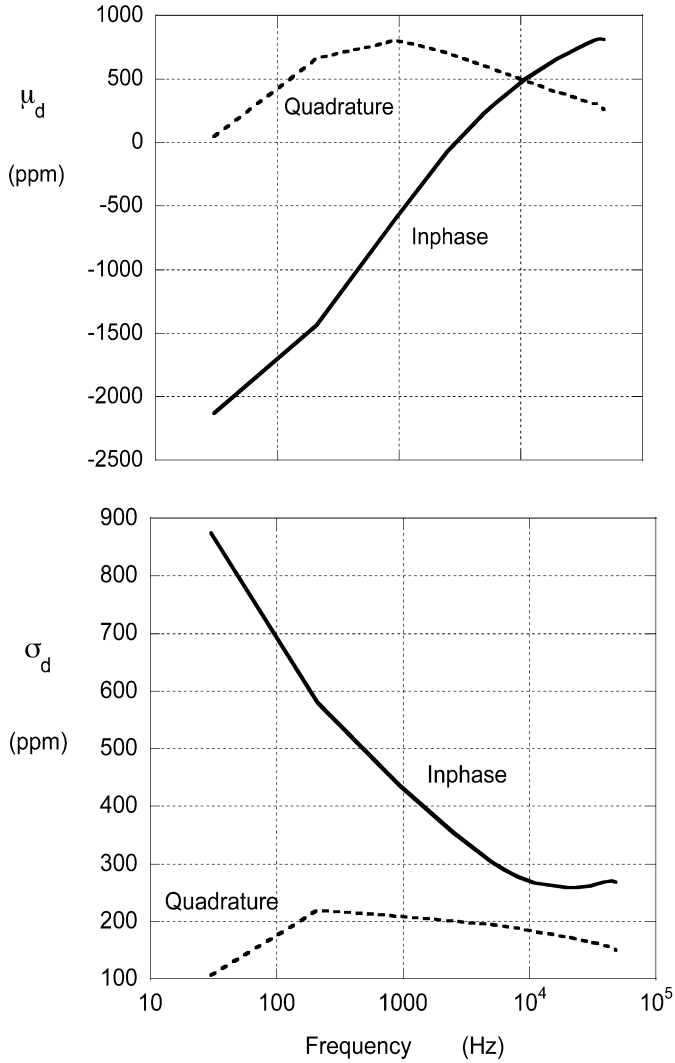


Fig. 18. (Top) Mean and (bottom) standard deviation of measurements over the clutter in Fig. 2, as functions of frequency.

$\mu_d(f)$ is subtracted from each $H_d$ value [see (25) and following discussion]. Here and in what follows $s_a$ and $s_b$ equal 0.5 and 2 cm, respectively. Fig. 19 shows that, when the target is shallow and the SCR is thus at its minimum, both the SLS and SWLS approaches do well. Greater target depths decrease the SCR, in the face of which the SWLS approach produces generally more consistent and more accurate results. Alternatively (Fig. 20), one may perform the same kind of test but keep the target at a fixed depth (20 cm from the center of target to clutter layer), while elevating the sensor. Here we scale $\mu_d$ and $\sigma_d$ with $h_r$ according to the $1/h_r^4$ and $1/h_r^5$ rules, respectively, where $h_r$ is depth relative to the initial value. The clutter $H_d$ values themselves are assumed to scale by $1/h_r^4$. Again, the SWLS approach produces more accurate and more stable results.

To extend the testing of the SWLS versus SLS approaches beyond the clutter data provided by the case treated above, further Monte Carlo runs were performed with clutter signals generated analytically by surface assemblages of small spheroids with assigned, randomized properties, locations, and orientations. Recently developed analytical solutions for EMI scattering from prolate and oblate spheroids now make this exercise possible [26]–[30]. Here the 36-cm long spheroidal target was

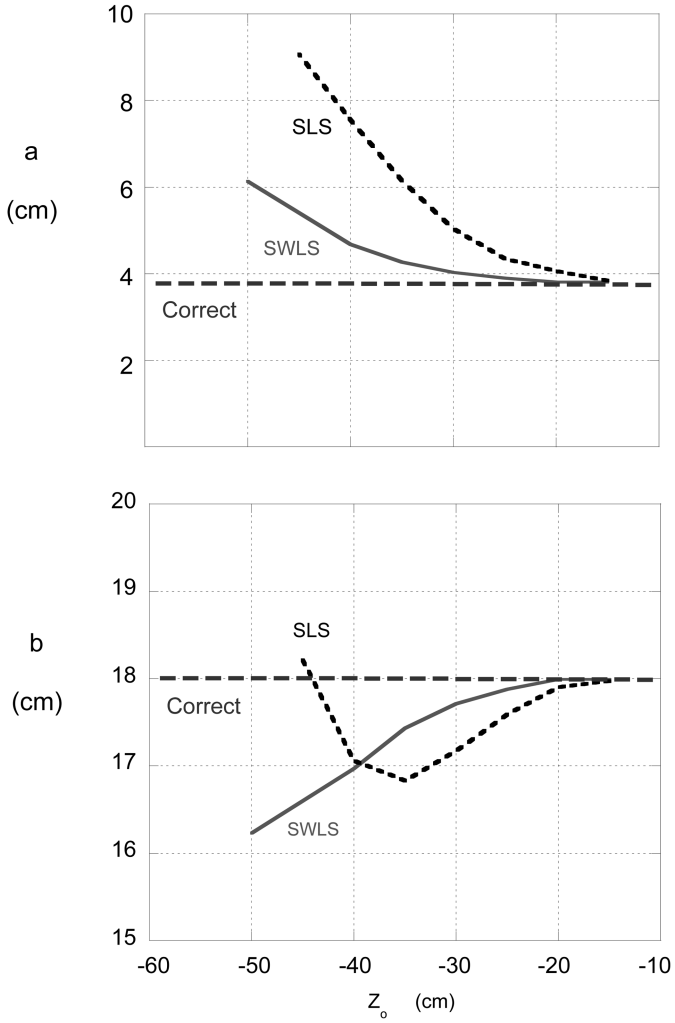


Fig. 19. Values of $a$ and $b$ obtained from inversion for different depths of target below the clutter.

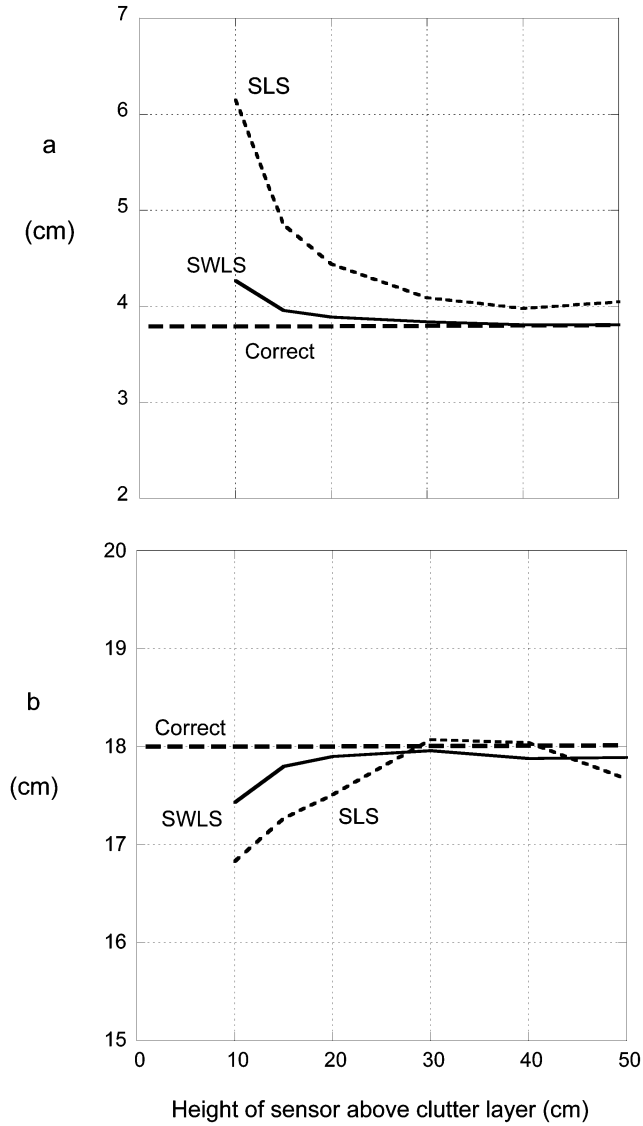


Fig. 20. Performance of SWLS versus SLS for characterizing a fixed UXO-sized object beneath the clutter in Fig. 2, for different antenna elevations above the clutter surface.

located 40 cm (to center) under the clutter layer and tilted at a 45° angle. $H_d$ was obtained directly from analytical calculation of scattered fields produced by the clutter particles and target, for the GEM-3 sensor at different elevations. To generate the signal clutter, 200 small spheroids ($a = 0.005$ m, $b = 0.03$ m, $\mu_r = 200, \sigma = 10^7$ s/m) were distributed on a $2 \times 2$ m square area, with random location and orientation for each spheroid. One hundred realizations of clutter distribution and orientation were calculated with several different sensor heights for each realization. For each realization data were obtained over a $5 \times 5$ grid with 10-cm (synthetic) measurement spacing, with both target and clutter present. Values of $a$ and $b$ were then inferred from the cluttered data. For each height, the signal mean value and standard deviation were calculated for the 100 realizations.

Not surprisingly, the mean values of $a$ and $b$ from both SLS and SWLS approaches are accurate, when $H_d$ corresponds to $H_d - \mu_d$ and a sufficient number of realizations is considered. However, the plot for standard deviation of $a$ and $b$ (Fig. 21) shows that the results from the SWLS approach are more stable and generally closer to the true value. For both approaches, raising the sensor reduces the standard deviation. This produces more accurate values of the parameters but in reality would produce signal magnitudes too faint to apprehend securely against other kinds of background noise.

## V. Summary Discussion

The specific strength and spectrum of EMI scattering from small, widely dispersed clutter items will depend on the particulars of the items and their distribution. At the same time, under various mild assumptions, simple power laws work well in describing the decline of received signal with antenna elevation. That pattern of decline is different from the sort we expect from larger discrete objects, i.e., targets of interest such as UXO. For dense, well-distributed clutter, direct application of the power laws works quite well. For sparse, heterogeneous clutter the theory also applies but in a statistical sense, i.e., on average over the measurement field. For a statistically homogeneous field, the deviation between data over an individual location and the ideal power laws declines as the sensor is elevated. Overall, raising the antenna should increase the signal-to-clutter ratio for all but the shallowest targets beneath a layer of clutter. Depending on the particulars of the case considered, the SCR advantage passes through a maximum as the antenna elevation

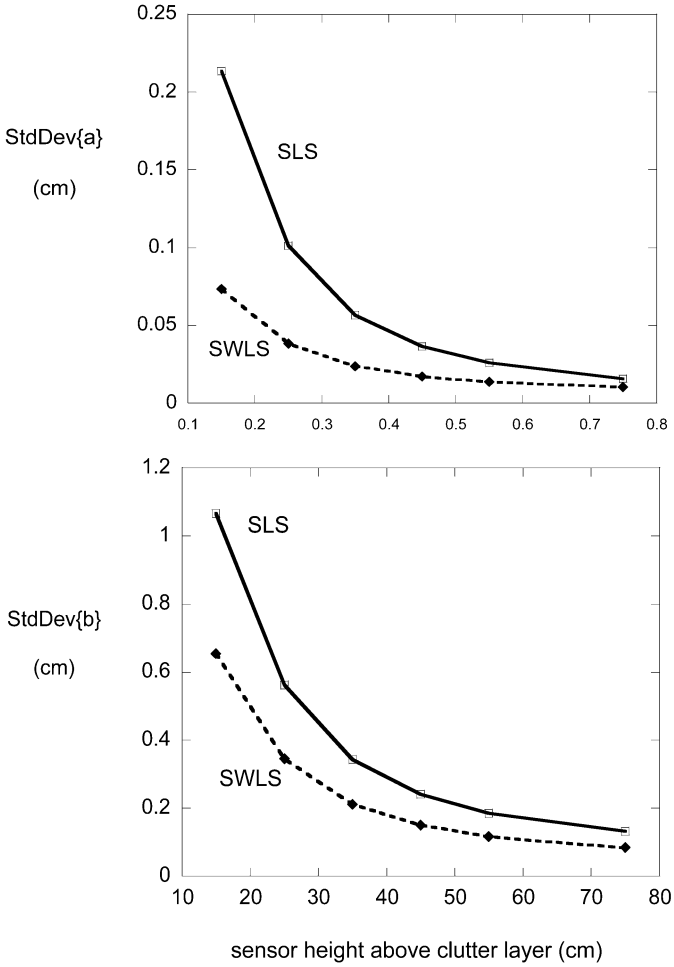


Fig. 21. Standard deviation of inferred $a$ and $b$ from 100 random realizations.

increases, and declines for greater elevation. The least advantage is gained under uniform primary fields. Bayesian-inspired data processing that takes advantage of the clutter statistics, including their elevation dependency, appears to be superior to simple least squares processing in discerning the properties of larger objects below a layer of clutter.

A few crucial concerns must enter into any treatment of data that attempts to exploit the results presented here. For sparse clutter, elevating the sensor causes the clutter signal variance to decrease as a percentage of the average magnitude of the clutter signal itself. While this is desirable overall, it can serve to amplify the role of weaker signals from higher elevations, when the variance is used to weight factors in the framework of statistical processing. Introducing an arbitrary noise floor will limit this, but leaves the task of selecting an appropriate floor value. The absolute diminution of signal strength with antenna elevation is itself a concern. EMI signals from dipole type antennas decline extremely rapidly with sensor elevation. The elevation at which signal fades to the level of background clutter and system noise depends on the specific sensor and the application considered. Future tests on specific sensors will illuminate this problem.

## ACKNOWLEDGMENT

An insightful anonymous reviewer provided perspective on logical ways to formulate spatial dependence of clutter density.

## REFERENCES

[1] I. J. Won, D. A. Keiswetter, D. R. Hanson, E. Novikova, and T. M. Hall, "GEM-3: A monostatic broad-band electromagnetic induction sensor," *J. Environ. Eng. Geophys.*, vol. 2, pp. 53–64, Mar. 1997.

[2] N. R. Carlson and K. L. Zonge, "Early time, multi-component mobile TEM for deep metal detection," presented at the *SAGEEP 2002*, Las Vegas, NV.

[3] J. M. Stanley and S. M. Griffin, "Sub-audio magnetics-simultaneous magnetic and electromagnetic detection of UXO," presented at the *UXO/Countermine Forum*, Orlando, FL, Sep. 3–6, 2002.

[4] D. D. Snyder, D. C. George, S. C. MacInnes, and K. L. Zonge, "Demonstration of a fast 4D TEM system at the NRL baseline ordnance test site," presented at the *UXO/Countermine Forum*, Orlando, FL, Sep. 3–6, 2002.

[5] T. H. Bell, B. Barrow, and N. Khadr, "Shape-based classification and discrimination of subsurface objects using electromagnetic induction," in *Proc. IGARSS*, vol. 1, Seattle, WA, Jul. 6–10, 1998, pp. 509–513.

[6] D. A. Keiswetter, I. J. Won, B. Barrow, and T. Bell, "Object identification using multifrequency EMI data," presented at the *UXO Forum*, Atlanta, GA, May 25–27, 1999.

[7] T. H. Bell, B. J. Barrow, and J. T. Miller, "Subsurface discrimination using electromagnetic induction sensors," *IEEE Trans. Geosci. Remote Sens.*, vol. 39, no. 6, pp. 1286–1293, Jun. 2001.

[8] S. C. MacInnes, D. D. Snyder, and K. L. Zonge, "Physics-based characterization of UXO from multicomponent TEM data," presented at the *UXO/Countermine Forum*, Orlando, FL, Sep. 3–6, 2002.

[9] L. M. Collins, P. Gao, N. Geng, L. Carin, D. Keiswetter, and I. J. Won, "Discrimination of UXO-like metal targets using wide-band electromagnetic induction," presented at the *UXO Forum*, Atlanta, GA, May 25–27, 1999.

[10] L. M. Collins, P. Gao, S. L. Tantum, J. Moulton, L. Makowsky, D. Reidy, and D. Weaver, "A comparison of statistical signal processing algorithms for detection and identification of low metal mines," presented at the *UXO Forum*, Anaheim, CA, May 2–4, 2000.

[11] P. Gao, L. M. Collins, P. M. Garber, N. Geng, and L. Carin, "Classification of landmine-like metal targets using wide-band electromagnetic induction," *IEEE Trans. Geosci. Remote Sens.*, vol. 38, no. 3, pp. 1352–1361, May 2000.

[12] Y. Zhang, L. M. Collins, H. Yu, C. Baum, and L. Carin, "Sensing of unexploded ordnance with magnetometer and induction data: Theory and signal processing," *IEEE Trans. Geosci. Remote Sens.*, vol. 41, no. 5, pp. 1005–1015, May 2003.

[13] D. J. Jackson, *Classical Electrodynamics*, 3rd ed. New York: Wiley, 1999.

[14] H. Braunisch, C. O. Ao, K. O'Neill, and J. A. Kong, "Magneto-quasistatic response of a distribution of small conducting and permeable objects," in *Proc. IGARSS*, vol. 4, Honolulu, HI, Jun. 24–28, 2000, pp. 1424–1426.

[15] F. Shubitidze, K. O'Neill, K. Sun, and I. Shamatava, "Interaction between highly conducting and permeable metallic objects in the low frequency EMI range," in *Proc. Applied Computational Electromagnetics Symp.*, Monterey, CA, Mar. 24–28, 2003, pp. 625–631.

[16] F. Shubitidze, K. O'Neill, K. Sun, I. Shamatava, and K. D. Paulsen, "Analysis of EMI scattering to support UXO discrimination: Heterogeneous and multiple objects," in *Proc. SPIE*, vol. 5089, Orlando, FL, Apr. 21–25, 2003, pp. 1035–1045.

[17] J. R. Wait, *Electromagnetic Wave Theory*, NY: Harper & Row, 1985.

[18] W. Hu, S. L. Tantum, and L. M. Collins, "EMI-based classification of multiple closely spaced objects via independent component analysis," *IEEE Trans. Geosci. Remote Sens.*, vol. 42, no. 11, pp. 2544–2554, Nov. 2004.

[19] L. M. Collins, P. Gao, S. L. Tantum, J. Moulton, L. Makowsky, D. Reidy, and D. Weaver, "A comparison of statistical signal processing algorithms for detection and identification of low metal mines," presented at the *UXO Forum*, Anaheim, GA, May 2–4, 2000.

[20] L. M. Collins, P. Gao, and L. Carin, "An improved Bayesian decision theoretic approach for land mine detection," *IEEE Trans. Geosci. Remote Sens.*, vol. 37, no. 2, pp. 811–819, Mar. 1999.

[21] K. Sun, K. O'Neill, I. Shamatava, and F. Shubitidze, "Application of prolate spheroid solutions in simulation of EMI scattering with realistic sensors and objects," in *Proc. Applied Computational Electromagnetics Symp.*, Monterey, CA, Mar. 24–28, 2003, pp. 531–537.

[22] K. Sun, K. O'Neill, I. Shamatava, F. Shubitidze, and K. D. Paulsen, "A fast forward model for simulating EMI scattering with realistic sensors and elongated objects," *J. Appl. Comput. Electromagn. Soc.*, vol. 18, no. 4, pp. 97–106, 2003.

[23] K. Sun, K. O'Neill, L. Liu, F. Shubitidze, I. Shamatava, and K. D. Paulsen, "Analytical solutions for EMI scattering from general spheroids with application in signal inversion for UXO discrimination," in *Proc. SPIE*, vol. 5089, Orlando, FL, Apr. 21–25, 2003, pp. 928–939.
[24] K. Sun, K. O'Neill, L. Liu, F. Shubitidze, and I. Shamatava, "Application of Bayesian inversion of scatterer shape from EMI data," presented at the *IEEE AP-S Int. Symp. USNC/CNC/URSI Nat. Radio Science Meeting*, Columbus, OH, Jun. 22–27, 2003.
[25] ——, "Application of Bayesian inversion of electromagnetic induction data for UXO discrimination," in *Proc. Symp. Applications Geophysics Engineering Environmental Problems (SAGEEP)*, San Antonio, TX, Apr. 6–10, 2003, pp. 1469–1478. 2003.
[26] I. Shamatava, K. O'Neill, F. Shubitidze, K. Sun, and C. O. Ao, "Evaluation of approximate analytical solutions for EMI scattering from finite objects of different shapes and properties," in *Proc. IGARSS*, vol. 3, Toronto, ON, Canada, Jun. 24–28, 2002, pp. 1550–1552.
[27] K. Sun, K. O'Neill, I. Shamatava, and F. Shubitidze, "Application of prolate spheroid solutions in simulation of EMI scattering with realistic sensors and objects," in *Proc. Applied Computational Electromagnetics Symp.*, Monterey, CA, Mar. 24–28, 2003, pp. 531–537.
[28] H. Braunisch, C. O. Ao, K. O'Neill, and J. A. Kong, "Magnetoquasistatic response of conducting and permeable prolate spheroid under axial excitation," *IEEE Trans. Geosci. Remote Sens.*, vol. 39, no. 12, pp. 2689–2701, Dec. 2001.
[29] C. O. Ao, H. Braunisch, K. O'Neill, and J. A. Kong, "Quasimagnetostatic solution for a conducting and permeable spheroid with arbitrary excitation," *IEEE-Trans. Geosci. Remote Sens.*, vol. 40, no. 4, pp. 887–897, Apr. 2002.
[30] B. E. Barrowes, K. O'Neill, T. M. Grzegorczyk, X. Chen, and J. A. Kong, "Broadband electromagnetic induction solution for a conducting and permeable spheroid," *IEEE Trans. Geosci. Remote Sens.*, vol. 42, no. 11, pp. 2479–2489, Nov. 2004.

**Kevin O'Neill** (M'98) received the B.A. degree (magna cum laude) from Cornell University, Ithaca, NY, and the M.A., M.S.E., and Ph.D. degrees from Princeton University, Princeton, NJ.

After a National Science Foundation Postdoctoral Fellowship at the Thayer School of Engineering, Dartmouth College, Hanover, NH, and the U.S. Army Corps of Engineers Cold Regions Research and Engineering Laboratory (CRREL), Hanover, he joined CRREL as a Research Civil Engineer. His research has focused on numerical modeling of porous media transport phenomena and of geotechnically relevant electromagnetic problems. He has been a Visiting Fellow in the Department of Agronomy, Cornell University, has continued since 1989 as a Visiting Scientist with the Center for Electromagnetic Theory and Applications, Massachusetts Institute of Technology, Cambridge, and since 1984 has been on the adjunct faculty of the Thayer School. His current research centers on electromagnetic remote sensing of surfaces, layers, and especially buried objects such as unexploded ordnance.

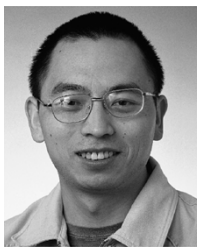

**Keli Sun** (M'03) received the B.S., M.S., and Ph.D. degrees in computational and biofluid mechanics from Peking University, Beijing, China, in 1991, 1994, and 1997, respectively, and the M.S. degree in computational electromagnetics from the Thayer School of Engineering, Dartmouth College, Hanover, NH, in 2001.

As an exchange student, he worked in the School of Pure and Applied Sciences, Tokyo University, Tokyo, Japan, from December 1995 to December 1996, studying the mobility and mechanical properties of membrane proteins in living cells. In 1997, he was a faculty member of Tsinghua University, Beijing, performing research and teaching biomechanics. He is currently a Research Associate in the Numerical Methods Laboratory, Thayer School, where he is furthering his research in computational electromagnetics and its applications in remote sensing, as well as algorithms for inverse problems.

**Fridon Shubitidze** (A'98–M'04) received the degree of Diploma radio physicist (M.S.) from the Sukhumi branch of Tbilisi State University (TSU), Republic of Georgia, in 1994 and the Cand.Sci. (Ph.D.) degree in radio physics (applied electromagnetics) from TSU, in 1997.

In 1994, he was a Member of the Research Staff of the Laboratory of Applied Electrodynamics, Department of Physics, TSU. At the same time, he joined Department of Physics and Mathematics, Sukhumi branch of TSU as a Senior Teacher and became Associate Professor there in 1998. From 1998 to 1999, he was a Postdoctoral Fellow with the National Technical University of Athens, Athens, Greece, performing research in connection with computer simulation of electrostatic discharge, electrodynamics aspects of EMC, numerical modeling of conformal antennas, electromagnetic wave scattering, field visualization and identification of objects by scattered field analysis, investigation of wave propagation through anisotropy, plasma, and chiral media, and innovative numerical methods. From June to August 2005, he was a Visiting Scientist in the Department of Earth and Ocean Science, University of British Columbia. He is currently a Research Scientist with the Thayer School of Engineering, Dartmouth College, Hanover, NH. His current work interests focus on numerical modeling of forward and inverse electromagnetic scattering by subsurface metallic objects, investigation of global magnetoquasistatic fields due to ionospheric currents, and electrostatic fields' effects on robotic and construction systems for Mars and Lunar exploration.

**Irma Shamatava** received the degree of Diploma radio physicist (M.S.) from the Sukhumi branch of Tbilisi State University, Tbilisi, Georgia, in 1994.

In 1997, she joined the staff of the Computer Center, Sukhumi branch of Tbilisi State University. During the same period, she was an Assistant Teacher in the Department of Physics and Mathematics. She is currently a Researcher with the Thayer School of Engineering, Dartmouth College, Hanover, NH. Her research interests focus on analytical and numerical modeling of electromagnetic scattering by subsurface metallic objects, especially unexploded ordnances.

**Keith D. Paulsen** (M'85) received the B.S. degree from Duke University, Durham, NC, and the M.S. and Ph.D. degrees from the Thayer School of Engineering, Dartmouth College, Hanover, NH, all in biomedical engineering.

He was an Assistant Professor in electrical and computer engineering at the University of Arizona, Tucson, and jointly, an Assistant Professor in radiation oncology with the Health Sciences Center, University of Arizona. He is currently a Professor of engineering at the Thayer School of Engineering. He has carried out sponsored research for the National Science Foundation, the National Cancer Institute, the Whitaker Foundation, and the National Institute of Health. He has published over 60 journal articles, over three dozen conference presentations, abstracts, and papers, and has contributed chapters on electromagnetic power deposition patterns to five books. At the Thayer School, he is Cofounder and Comanager of the Numerical Methods Laboratory. He performs research and teaches courses in computational methods for engineering and scientific problems, with particular applications in electromagnetics, subsurface object sensing, and biomedical engineering.

Dr. Paulsen is the recipient of numerous academic and research awards and fellowships. He has served on more than ten advisory committees for the National Cancer Institute and has chaired or organized five symposia on hyperthermic cancer treatment.